PHILOSOPHICAL TRANSACTIONS A

rsta.royalsocietypublishing.org

Research

Article submitted to journal

Subject Areas:
Taylor–Couette and Related Flows on the Centennial of Taylor's Seminal Philosophical Transactions Paper

Keywords:
Fluid Dynamics, Bifurcations, Numerical Methods, Experiments

Author for correspondence:
Francisco Marques
e-mail: francisco.marques@upc.edu

Stably Stratified Taylor–Couette flows

Jose M. Lopez[1], Juan M. Lopez[2] and Francisco Marques[1]

[1]Departament de Física Aplicada, Universitat Politècnica de Catalunya, Barcelona 08034, Spain
[2]School of Mathematical and Statistical Sciences, Arizona State University, Tempe AZ 85287, USA

Stably stratified Taylor–Couette flow has attracted much attention due to its relevance as a canonical example of the interplay between rotation, stable stratification, shear and container boundaries, as well as its potential applications in geophysics and astrophysics. In this paper, we review the current knowledge on this topic, highlight unanswered questions and propose directions for future research.

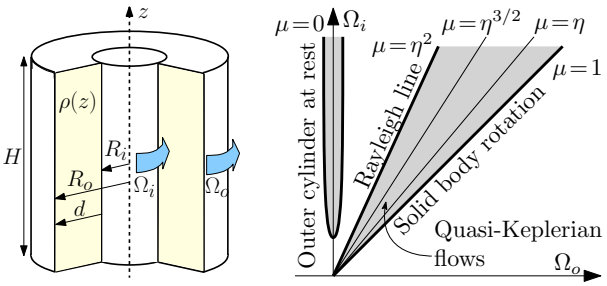

The figure on the left is a schematic of the Taylor–Couette apparatus, filled with fluid of kinematic viscosity ν and initial density stratification $\rho(z)$. The nondimensional parameters come in three groups. Geometric parameters: the radius ratio $\eta = R_i/R_o$ and the aspect ratio $\gamma = H/d$; for axially periodic flows with wavenumber k, $H = 2\pi/k$. Dynamic parameters: the Reynolds number $Re = \Omega_i R_i d/\nu$, the rotation ratio $\mu = \Omega_o/\Omega_i$, and the Froude number $Fr = \Omega_i/N$, where $N = \sqrt{g\rho_0^{-1} d\rho(z)/dz}$ is the Brunt–Väisälä buoyancy frequency, ρ_0 is the mean density and g is the gravitational acceleration. Fluid parameters: the Prandtl number $Pr = \nu/\kappa$ for temperature stratification, or the Schmidt number $Sc = \nu/D$ for solute concentration stratification, where κ and D are the thermal and mass diffusivities. The figure on the right shows the parameter regions in grey that will be discussed.

Royal Society Publishing

1. Introduction

The dynamics of Taylor–Couette flow has been extensively studied since the pioneering work of [1]. It has become a canonical model for the study of nonlinear dynamics, bifurcations and symmetries in fluid dynamics. Interests in stably stratified Taylor–Couette flows have developed more recently, ranging from understanding the fundamentals of the dynamics in a realizable laboratory flow, its relevance as a canonical example of the interplay between rotation, stable density stratification, velocity shear and horizontal boundaries, to potential applications in geophysics and astrophysics. The stratifying agent may be either temperature or solute concentration (typically salt). The equations and the corresponding dynamics are essentially the same in both cases, but the corresponding diffusivities differ by three orders of magnitude. Moreover, the experimental boundary conditions for temperature and salt are usually different. On the annular sidewalls, the boundary conditions for temperature and salt concentration are the same, zero wall-normal flux, but they typically differ on the top and bottom endwalls. It is not possible to fix the salt concentration at the endwalls (the physical condition is zero wall-normal flux, as on the sidewalls), while with temperature it is the easiest condition to impose. In addition, experiments using salt stratification have buoyancy boundary layers on the endwall (due to the zero flux condition) that grow very slowly, eventually leading to uniform concentration throughout the annulus.

For the sake of definiteness, we will discuss the governing equations for the temperature stratification case, illustrated in figure 1(a). The non-dimensional governing equations, using the annular gap d as the length scale, the viscous diffusion time d^2/ν as the time scale and the temperature difference between top and bottom lids ΔT^* as the temperature scale, in the Boussinesq approximation and accounting for centrifugal buoyancy [2], are

$$(\partial_t + \boldsymbol{u}\cdot\boldsymbol{\nabla})\boldsymbol{u} = -\boldsymbol{\nabla}p + \nabla^2\boldsymbol{u} + Gr\,T\hat{\boldsymbol{z}} + \epsilon\,T(\boldsymbol{u}\cdot\boldsymbol{\nabla})\boldsymbol{u}, \tag{1.1}$$

$$(\partial_t + \boldsymbol{u}\cdot\boldsymbol{\nabla})T = Pr^{-1}\nabla^2 T, \quad \boldsymbol{\nabla}\cdot\boldsymbol{u} = 0, \tag{1.2}$$

where $\epsilon = \alpha\Delta T^*$ is the relative density variation, α is the coefficient of volume expansion, and $Gr = \alpha g \Delta T^* d^3/\nu^2$ is the Grashof number. The term $\epsilon\,T(\boldsymbol{u}\cdot\boldsymbol{\nabla})\boldsymbol{u}$ accounts for centrifugal buoyancy effects. The Brunt–Väisälä buoyancy frequency is $N = \sqrt{\alpha g \Delta T^*/H} \propto \sqrt{Gr}$. Notice that Gr and ϵ are both proportional to the imposed temperature gradient, and their ratio, the Archimedes number $Ar = Gr/\epsilon = gd^3/\nu^2$, is fixed for a given experimental setting. Therefore, ϵ is not an independent parameter, but depends on Gr via the fixed Archimedes number: $\epsilon = Gr/Ar$.

The boundary conditions for temperature and velocity are:

$$r = r_i: \qquad \partial T/\partial r = 0, \qquad u = w = 0,\ v = Re, \tag{1.3a}$$

$$r = r_o: \qquad \partial T/\partial r = 0, \qquad u = w = 0,\ v = \mu Re/\eta, \tag{1.3b}$$

$$z = -\gamma/2: \qquad T = -1/2, \qquad u = w = 0,\ v = q_b(r), \tag{1.3c}$$

$$z = \gamma/2: \qquad T = 1/2, \qquad u = w = 0,\ v = q_t(r), \tag{1.3d}$$

where q_t and q_b are the top and bottom endwall velocities, and depend on the specifics of the experiment or simulation model considered: the endwalls may be fixed, attached to the inner or outer cylinder, or periodic boundary conditions in the axial direction may be used in model simulations. Notice that Re and μ enter into the problem via the boundary conditions.

The governing equations and boundary conditions are equivariant under the mid-plane reflection (Boussinesq symmetry), assuming $q_t = q_b$, whose action is

$$\mathcal{K}: [u, v, w, T](r, \theta, z, t) \mapsto [u, v, -w, -T](r, \theta, -z, t), \tag{1.4}$$

if not for the centrifugal buoyancy term $\epsilon\,T(\boldsymbol{u}\cdot\nabla)\boldsymbol{u}$; ϵ is a measure of the strength of the centrifugal term. The denser fluid near the bottom endwall is centrifuged radially outwards, while the lighter fluid near the top endwall is centrifuged inwards, generating a large scale circulation

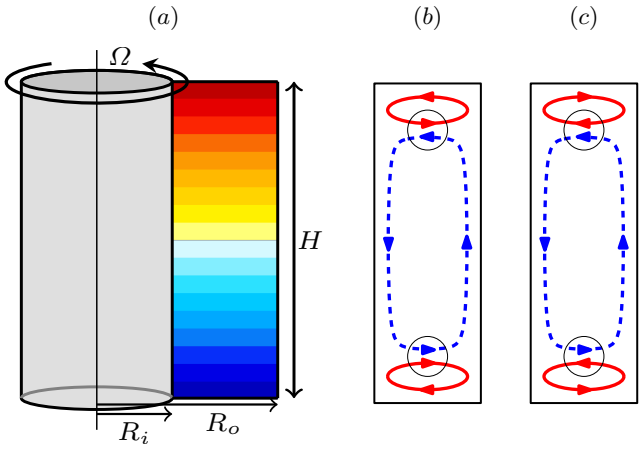

Figure 1. (a) Schematic of the stratified Taylor–Couette device showing the density stratification. (b) Schematic of the large scale circulation (blue) and Ekman vortices (red) in finite stratified Taylor–Couette flow; the top and bottom endwalls are fixed to the stationary outer cylinder. (c) Same as (b) but with the endwalls attached to the rotating inner cylinder.

that breaks $\mathcal{K}$, as illustrated schematically in figure $1(b)$, when endwalls are fixed to the stationary outer cylinder ($\mu = 0$) and in figure $1(c)$ when endwalls are fixed to the rotating inner cylinder.

There are several instabilities in stratified Taylor–Couette flow. One is centrifugal instability due to the rotation of the inner cylinder. The formation of Ekman vortices near the endwalls, due to the differential rotation of the endwalls is another source of instabilities. The shear due to the differential rotation between the cylinders and the centrifugal buoyancy term are additional sources of instabilities. Finally, all these mechanisms are strongly modified by the presence of a vertical stabilizing density gradient. Which one of these mechanisms is responsible for the instability of the base flow depends critically on the geometry (radius ratio and aspect ratio) and the different strengths of these mechanisms for different parameter values (Reynolds and Froude numbers, rotation ratio and diffusivity ratio). This review paper is organized in two blocks, one concerning on the instabilities in the classical Taylor–Couette setting, with the outer cylinder at rest, and the other considers the strato-rotational instability (SRI) in centrifugally stable flows. The corresponding parameter regimes are shown in the figure in the preamble on the first page. Additionaly, in the Perspective final section, other horizontal shear flows with vertical stratification, which are the subject of growing interest today, are discussed.

2. Stratified Taylor–Couette flows with the outer cylinder at rest

One of the first theoretical analysis of stratified Taylor–Couette flow was [3], who used highly idealized model equations and found that stratification resulted in a higher critical Reynolds number for instability, along with a reduced axial wavelength for the resulting Taylor vortices. The analysis was restricted to flows with a stationary outer cylinder, and the idealizations of the linear stability analysis included restricting to axisymmetric modes and assuming axial periodicity. Some of the first experiments in Taylor–Couette flows with axial stratification were conducted by [4]. Their apparatus had a small radius ratio ($\eta = 0.2$), linear density gradients, and several rotation rates of the cylinder were used. With increasing density gradient, instability was inhibited, with onset occurring at larger Reynolds numbers. The bifurcated state was a (non-axisymmetric) rotating wave which had a cellular-like structure of substantially shorter axial extent than the Taylor cells found in unstratified experiments (see figures 5 and 6 of [4]). In a subsequent study [5], they tried to explain their experimental observations using linear stability analysis. The results were not satisfactory due to the idealizations used: they considered only axisymmetric perturbations, and assumed axial periodicity of the flow. Nevertheless, two general

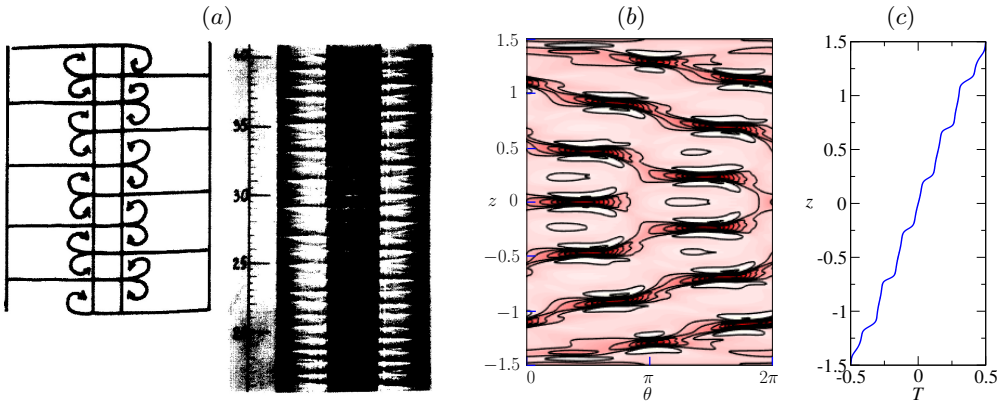

Figure 2. (a) Stratified Taylor–Couette flow with outer cylinder at rest and $\eta \sim 0.4$; experimental shadowgraph and its schematic interpretation (reproduced from [6] with permission of the publisher). (b) DNS at $Re = 800$, $Fr = 0.53$, $\eta = 0.417$ and $\gamma = 3$ showing contours of axial temperature gradient in an (θ, z) cylindrical plane at 1% gap distance from the inner cylinder (reproduced from [7] with permission of the publisher). (c) Temperature profile of (b) at the same radial distance from the inner cylinder and $\theta = \pi/2$.

experimental observations were borne out: the linear density gradient inhibits onset of instability, and the axial wavelength of the instability cells is diminished.

Several subsequent studies [6,8–11] explored stratified Taylor–Couette flows in detail via linear stability analyses, nonlinear simulations, and experiments over a wide range of parameters. They considered annuli with $\eta \sim 0.8$ and $\gamma \sim 50$, and found experimentally that linear density gradients inhibit instability, that the bifurcated state is generally unsteady, non-axisymmetric, and with a reduced axial length scale, as can be seen in figure 6 of [6] (reproduced here in figure 2a). They observed that instability originates at the inner cylinder and propagates toward the outer cylinder in the form of pairs of vortices. The fluid between the cylinders is well mixed, and a density interface with substantial gradients forms in the horizontal planes between the sets of vortex pairs. The vortex pairs on diametrically opposite sides of the inner cylinder are shifted vertically by a half axial wavelength (the height of one vortex). How these diametrically opposed vortex pairs join together was not clear from their observations. The whole pattern rotated with a constant velocity less than Ω_i.

The modelling efforts of [6,8] were unable to reproduce the experimentally observed oscillatory and non-axisymmetric instability. This, again, was due to the idealizations used to make the analysis tractable. The basic state considered in the modelling was the unidirectional circular Couette flow of [1],

$$v = Ar + B/r, \tag{2.1}$$

where v is the azimuthal component of velocity and the constants A and B depend on η and Re, together with a linear vertical stratification, and only allowed for axisymmetric and axially periodic instability modes. The axisymmetric restriction was relaxed in [9], and they found primary instabilities to non-axisymmetric modes with azimuthal wavenumbers $m = 1$, 2 or 3, depending on the parameter regime. They found that these modes are not spirals, but instead were similar to the structures experimentally observed in [6]. In [7], the experimental results were reproduced by direct numerical simulations (DNS), which showed that endwall effects and symmetries are critical ingredients for understanding the observed onset of instability and subsequent dynamics. This series of studies suggests that the large-Prandtl (or Schmidt) number limit is approached when $Pr \gtrsim 10$.

Subsequent experiments were conducted by [13] with the goal of analyzing the robustness of the density layers found in the experiments of [8]. These experiments used an apparatus with smaller η and γ parameters, larger Re and considering both linearly and discretely stratified flows.

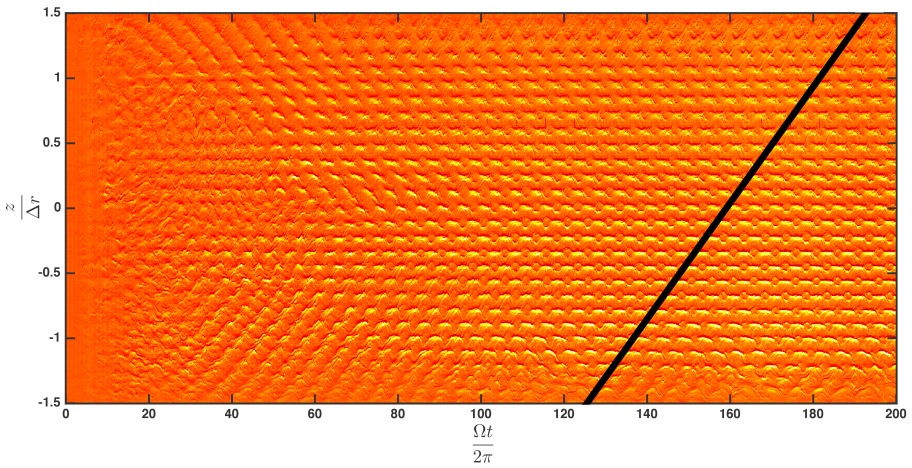

Figure 3. Time series of a shadowgraph visualisation from an experiment with an initial linear stratification for $Re = 7000$, $Fr = 0.05$, $\eta = 0.417$, $\gamma = 1.5$, and $Sc = 700$; the regions of high contrast show the locations of sharp density interfaces (reproduced from [12] with permission of the publisher).

Additional experiments followed, with more sophisticated data acquisition techniques, and focusing on the linearly stratified case with parameter values $\eta \sim 0.4$ and $\gamma \sim 3$ [12,14–16]. They observed the density interface using shadow-graph visualization, and reported that the density interfaces are of an intermittent nature, mixing periodically. Figure 3 shows an example of such a space-time shadowgraph. They performed a linear stability analysis of the unidirectional Taylor–Couette flow (2.1). The linear stability analysis failed to reconcile the axial distance observed in the experiment between the sharp density gradients. Subsequent nonlinear simulations, assuming an infinitely long annulus periodic in the axial direction, showed that the onset of instability breaks axisymmetry. The resulting flow structures have much in common with those reported in [9]. According to [14], the absence of endwalls in these nonlinear numerical simulations may be responsible for the differences between the simulated structures and those observed experimentally. The experiments of [16] suggest that the axial wavelength (the distance between the density layers) does not depend on the gap between the cylinders d, but rather depends on the thickness of the boundary layer close to the rotating inner cylinder.

The experiments [14–16] on linearly stratified Taylor–Couette flows used salt as the stratifying agent, and parameter values $\eta = 0.417$ and $\gamma = 3$. These experiments motivated a DNS study [7] that reproduced these results and shed light on the instability mechanisms and flow structure. The governing equations for the DNS study are (1.1) and (1.2), and the parameter values $\eta = 0.417$, $\gamma = 3$, $Ar = 10^{10}$ and $Fr = 0.53$ were fixed. Varying Re gives $Gr = 20.8754\,Re^2$ and $\epsilon = 2.087\,54 \times 10^{-9}\,Re^2$; ϵ is small, of order 10^{-2} for $Gr \sim 10^8$. The steady axisymmetric base state is essentially $\mathcal{K}$ symmetric. The centrifugal buoyancy effects near onset of instability are almost negligible. The basic state loses stability at $Re \approx 320$ via a Hopf bifurcation breaking $SO(2)$ symmetry, leading to a rotating wave R_1 with azimuthal wavenumber $m = 1$, that is stable up to $Re \approx 1000$. The 3D structure is very similar to that found in the experiments [6], and illustrated in figure 2(b), that shows contours of the axial temperature gradient $\partial_z T$ on a cylindrical surface near the inner cylinder at 10% of the gap. Wide regions of almost constant temperature ($\partial_z T \approx 0$, the white regions in the figure) alternate with narrow regions of fast variation in T in an axially periodic way for $\theta \in (0, \pi)$. In the other half of the cylinder, for $\theta \in (\pi, 2\pi)$, the same structure is found, but shifted axially by half an axial wavelength. In between there is a narrow dislocation region where both structures meet. The temperature profile near the inner cylinder shows a well defined stair-case structure (see figure 2c).

Since the solution is a rotating wave, the temperature gradient plot in (θ, z) at an instant in time at a given radius (figure 2b) is identical to a space-time plot with $\theta \in [0, 2\pi]$ replaced

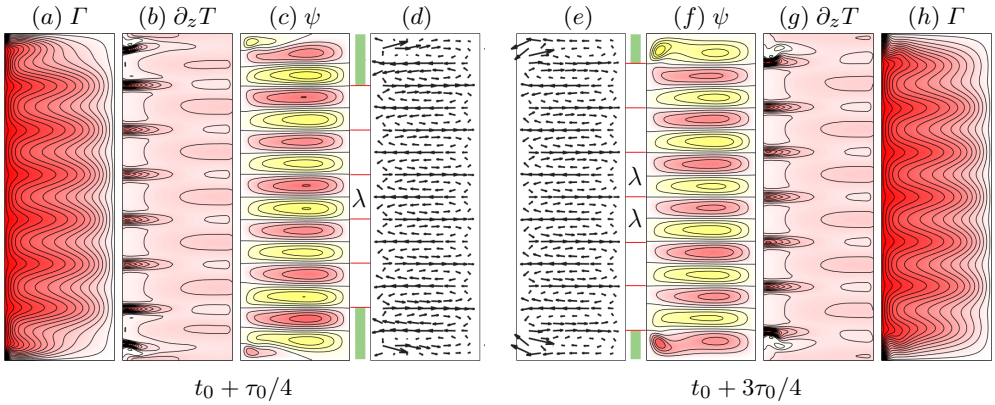

Figure 4. Rotating wave at $Re = 800$, showing contours of angular momentum $\Gamma = rv$, axial temperature gradient $\partial_z T$, streamfunction ψ and velocity vectors projected onto a meridional plane for the angles $\theta = \pi/2$ and $3\pi/2$ in figure 2(b), where the outgoing radial jets are strongest (reproduced from [7] with permission of the publisher).

by time over one rotation period. When solving the governing equations in the axisymmetric subspace, the first instability is instead to an axisymmetric periodic solution, whose space time plot (contours of $\partial_z T$ in a (t, z) plane for fixed r near the inner cylinder) is almost identical to figure 2(b). The study of both the 3D rotating wave and the axisymmetric limit cycle provide the same information for the states appearing at the first bifurcation. Figure 4 shows contours of angular momentum $\Gamma = rv$, axial temperature gradient $\partial_z T$, streamfunction ψ and velocity vectors projected onto a meridional plane of the rotating wave in figure 2(b) for the angles $\theta = \pi/2$ and $3\pi/2$, away from the defect regions at $\theta = 0$ and π. The jets of angular momentum emerging from the inner cylinder due to the centrifugal instability have maximum intensity for $\theta = \pi/2$ (h) and $3\pi/2$ (a). The regions with large temperature gradient shown in (b, g) coincide with the jets of angular momentum. These jets are periodically spaced with wavelength λ, except near the endwalls where Ekman vortices exist. Between the jets are a pair of counter rotating Taylor vortices (c, d, e, f), forming a Taylor cell of length λ. The Taylor vortices are very elongate radially, substantially shorter in the axial direction than the Taylor vortices the absence of stratification, which have $\lambda \approx d$. The Ekman vortices at the endwalls change size in order to accommodate the different number of cells that exist in the two regions separated by the defect regions, and play a subordinate role in the dynamics.

The DNS analysis in this problem, with $\eta \sim 0.4$, shows that the physical mechanism responsible for the instability of the base state is the centrifugal instability, and the Ekman layers play a secondary role. Moreover, the centrifugal buoyancy does not play any role in the primary bifurcation. The DNS results fully agree with the afore mentioned experiments for the gap $\eta \sim 0.4$.

A recent experimental investigation [17] of stratified Taylor–Couette flow with a very small radius ratio $\eta \approx 0.066$ and using salt as stratifying agent, found that at the onset of instability spiral structures confined to the inner rotating cylinder appear, and the spiral near the bottom endwall is being triggered first. This was a very different regime to that typically studied for stratified Taylor–Couette flow discussed up to now. In [18], the experimental results were reproduced by DNS, showing that endwall and centrifugal buoyancy effects are critical ingredients for understanding the observed onset of instability and subsequent dynamics.

The spiral structures observed in [17] resemble the radiative instability (RI) reported by [19]. These authors placed a rotating cylinder in a large rectangular tank filled with a stratified fluid using salt as stratifying agent. [20] analized the RI and showed, using the approximation of large axial wavenumber, that RI and the strato-rotational instability (SRI) are related: the SRI transforms into RI when the cylinder's gap d becomes large enough. Along with their experiments, [19] studied the linear stability analysis of the potential flow around an isolated infinitely long rotating cylinder placed in a linearly stratified medium. The velocity field of the potential flow has

azimuthal component $v \propto 1/r$, zero meridional components $u = w = 0$, and extends radially out to $r \to \infty$. They considered the flow inviscid, and presented some comments on viscous effects. The main mode of instability was found to result in helical waves with azimuthal wavenumbers that depend on *Fr* and *Re*. Their experiments were conducted in a tank of depth $48\,\mathrm{cm}$ and horizontal cross section $240\,\mathrm{cm} \times 74\,\mathrm{cm}$, filled to a height of $45\,\mathrm{cm}$. They used three different cylinders of radii $R_i = 12.5$, 15 and $20\,\mathrm{cm}$. They observed instabilities typically consisting of helical waves travelling up from the bottom and down from the top. They expected the flow to have the reflection symmetry $\mathcal{K}$ about the horizontal mid- plane, but found in some cases that one of the two waves could be dominant, and that there was a difference between the frequencies of the two waves together with a slow drift toward the top. They also observed that the buoyancy frequency was not uniform across the fluid depth, with departures mostly located at the top and bottom lids in a region $10\,\mathrm{cm}$ deep, which they ascribed to salt diffusivity, evaporation effects and turbulent mixing. Centrifugal buoyancy effects were not considered as a potential contributor to any of these observations.

Centrifugal buoyancy effects in stratified Taylor–Couette flows have been neglected in most of the studies. However, [21] suggested that centrifugal buoyancy effects may not be negligible, and [22] raised the cautionary point that the use of the Boussinesq approximation without centrifugal buoyancy seems to still be an open question for small Froude numbers. [23] considered the possible contribution of centrifugal buoyancy in their experiments, and concluded that they could neglect this contribution because $R_i\Omega_i^2/g$ is small for the parameter regimes used in the experiments. They also studied the linear stability of the unidirectional stratified Taylor–Couette flow periodic in the axial direction, and found discrepancies between the model and experimental results. They assumed the discrepancy would be due to ignoring endwall effects in their model, but did not pursue this as it was beyond the scope of their study.

So far, the theoretical studies of stratified Taylor–Couette flow [9,22–27] have considered the axial direction to be periodic and the base state to be the unidirectional flow of [1], equation (2.1), together with a linear vertical stratification. However, all physical experiments have finite axial length, and differential rotation between the top and bottom lids and the cylinders exists. Moreover, the top endwall is sometimes open. This leads to vortex line bending near one or both corners where the rotating inner cylinder meets the stationary bottom and top endwalls, driving a secondary meridional flow, the so called Ekman vortices near the lids. Therefore the base flow is not unidirectional. This meridional flow is a critical ingredient in determining the helical instability reported in the experiments of [17].

Figure 5(a) shows a visualization of the flow from the experiments of [17] at $\eta = 1/15$, displaying only a region very close to the inner cylinder. They found helical wave structures confined to the inner cylinder in regimes where the Froude number is less than one. These helical waves were reported to originate at the corners where the inner cylinder meets the top and bottom boundaries, and were found to be asymmetric with the lower helical wave being more intense. The DNS in [18] reproduced these results and found that endwall effects and centrifugal buoyancy were critical ingredients for understanding the observed onset of instability and the subsequent dynamics.

In a given experiment, *Gr* and ϵ are kept fixed, while the Froude number $Fr \propto Re/\sqrt{Gr}$ varies when the rotation rate of the inner cylinder changes. The fixed parameter values in the experiment [17] and numerical simulations [18] are $\eta = 0.07$, $\gamma = 1$, $\epsilon = 0.064$ and $Gr = 4 \times 10^{10}$, with $Pr = 6$ for the thermally stratified DNS and $Sc \approx 700$ for the salt stratified experiments. This results in $Ar = Gr/\epsilon = 6.25 \times 10^{11}$. Notice that in this small $\eta = 0.07$ case, the Archimedes number is almost two orders of magnitude bigger (and ϵ one or two orders of magnitude bigger, depending on *Re*) than in the $\eta = 0.417$ cases discussed earlier.

The centrifugal buoyancy term generates a large scale circulation that breaks the reflection symmetry $\mathcal{K}$, illustrated in the schematics on figure 1(b). This large scale circulation reinforces the Ekman vortex at the bottom lid, and weakens the Ekman vortex at the top lid when the endwalls are stationary. The maximum value of the radial velocity u in the bottom boundary

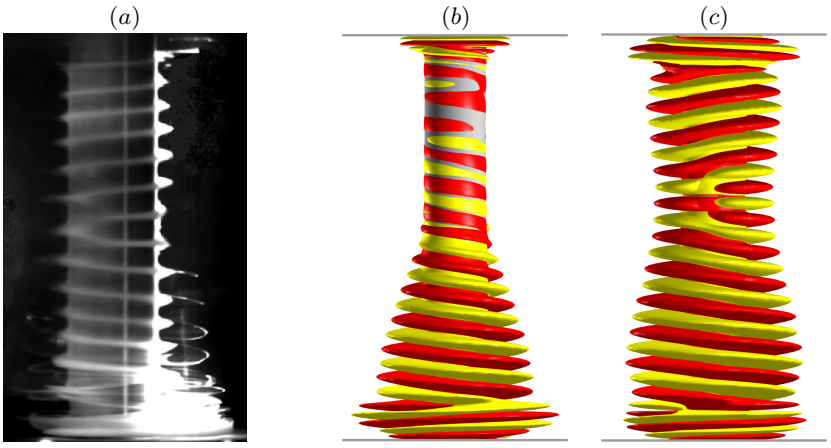

Figure 5. (a) Dye visualization of two helical waves travelling along the rotating inner cylinder from the top and bottom (reproduced from [17] with permission of the publisher).(b) DNS at $Re = 6100$, $Fr = 0.4052$, $Pr = 6$, $\eta = 0.07$ and $\gamma = 1$, showing isosurfaces of helicity density; (c) same as (b) but at $Re = 6500$ and $Fr = 0.4318$ (reproduced from [18] with permission of the publisher).

layer is approximately 10% larger than the maximum value of u in the top boundary layer, for the base state close to the first bifurcation [18]. This is in marked contrast with the $\eta = 0.417$ case discussed earlier, where centrifugal buoyancy effects were negligible; in that case ϵ was two orders of magnitude smaller near the instability threshold.

The basic state undergoes a supercritical Hopf bifurcation to a rotating wave with $m = 1$ and frequency ω_1. This happens at $Re \approx 5970$, which is smaller (approximately 2%) than the critical Re when $\epsilon = 0$. The bifurcated state, shown in figure 5(b) at $Re = 6100$, clearly has no symmetry in z. The instability takes place at the bottom Ekman vortex near the inner corner and progresses upwards, while the top Ekman layer remains stable, due to the centrifugal buoyancy mechanism already discussed. Increasing the Reynolds number to $Re \approx 6220$, a helical wave appears at the top of the cylinder. Both helical waves meet near the cylinder mid-plane, but a little closer to the top endwall. The helical wave on the lower half of the cylinder is more intense, and their frequencies are slightly different. They both rotate prograde with the inner cylinder, but the bottom helical wave rotates slightly faster than the top helical wave. This results in a modulated rotating wave state MRW. Most of the dynamics takes place near the inner cylinder. A snap-shot of MRW at $Re = 6500$ is shown in figure 5(c). This state closely resembles the experimental flow obtained by [17], shown in figure 5(a), that corresponds to $Re \approx 6920$. Further increasing Re results in additional bifurcations resulting in spatio-temporal complex flows [18]. The DNS analysis of [18] has shown that the instabilities of the Ekman vortices are the underlying mechanism, and the lack of reflection symmetry is due to the centrifugal buoyancy. This is in marked contrast with the case discussed before with gap $\eta \sim 0.4$ and a smaller ϵ value.

3. Strato-rotational instability in centrifugally stable flows

A major breakthrough in the study of stably stratified Taylor–Couette flow was the realization that the region of linear instability extends beyond the Rayleigh line ($\mu > \eta^2$), thereby including rotation laws which are centrifugally stable according to the Rayleigh criterion. This characteristic was first reported by [28,29], who conducted a modal stability analysis of the inviscid equations and found that a sufficient condition for instability is $\mu < 1$, i.e. the angular velocity must decrease radially outwards. They observed that the Couette flow becomes unstable as a result of a pitchfork bifurcation, leading to non-axisymmetric and non-oscillatory structures (see figure 6a), which are markedly distinct from the Taylor vortices and spirals observed in the centrifugally

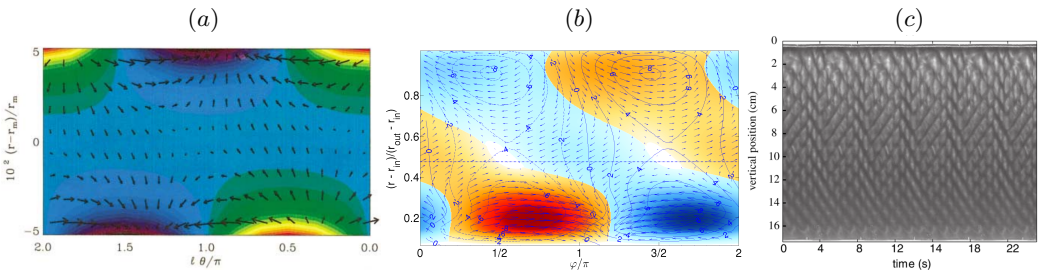

Figure 6. (a) The most unstable eigenmode obtained from linear stability analysis for $Fr = 0.01$, $\mu = 0.5812$, $\eta = 0.67$ and $Re = 75\,450$ (reproduced from [28] with permission of the publisher). The arrows indicate the radial and azimuthal velocities. The axial velocity is shown in color where upward (downward) motion corresponds to red (blue) regions. The vertical axis shows the radial direction, rescaled and normalized with the mean radius, $r_m = 0.5(r_i + r_o)$, whereas the abscissa shows the azimuthal direction. (b) Colour map of velocity perturbations showing the structure of the $m = 1$ mode of the SRI in experiments conducted at $\mu = 0.463$, $Re = 600$, $Fr = 2$, $\eta = 0.5172$ and $R_n = 289$, where $R_n = Nr_i(r_o - r_i)/\nu$ is the Brunt–Väisälä number. Prograde and retrograde flow are shown as red and blue, respectively. As in (a), the vertical and horizontal axes show the radial and azimuthal directions, respectively. Note that here the radial direction is rescaled with the inner cylinder radius, r_i, and normalized by the gap size, $r_o - r_i$ (reproduced from [31] with permission of the publisher). (c) Space-time diagram obtained from experimental visualizations illustrating the pattern of interpenetrating spirals characteristic of SRI in the centrifugally stable regime (reproduced from [32] with permission of the publisher).

unstable regime ($\mu = 0$) discussed in the previous section. The height-to-width aspect ratio of these structures was found to be proportional to Fr, so that their axial extent becomes increasingly smaller as the stratification level increases. [30] revisited the problem using several methodologies, including the Wentzel–Kramers–Brillouin (WKB) approximation and numerical simulations, and confirmed the stability threshold proposed by [28]. This study also showed that the primary instability may occur through a Hopf bifurcation, resulting in non-axisymmetric oscillatory modes. More recently, [25] showed that stably stratified flows may also become unstable when the outer cylinder rotates faster than the inner cylinder, extending the instability criterion to $\mu \neq 1$, i.e. all rotation laws except for solid-body rotation. However, unlike cases with $\mu < 1$, where the flow becomes unstable for a wide range of Fr, for $\mu > 1$ the instability only sets in if the flow is strongly stratified. Although all these theoretical studies were performed in the inviscid limit, they verified numerically that the instability persists for a finite viscosity.

Linear stability analysis including the viscous term was first performed by [22]. They considered a fixed value of the Froude number, $Fr = 0.5$, and two values of the radius ratio, $\eta = 0.3$ and $\eta = 0.78$, to examine the instability in small and wide gap configurations. The region of instability was in both cases delimited by $\mu \lesssim \eta$, a threshold that was much more restrictive than that obtained in [28]. However, a subsequent study by the same authors [33] revealed that such a threshold may vary depending on the stratification level and the curvature of the apparatus, especially when the narrow or wide gap limits are approached. They observed that for values of η close to the small gap limit ($\eta \to 1$), the critical threshold approaches the solid-body rotation line ($\mu = 1$), in agreement with the inviscid study of [28]. In contrast, if the wide gap limit is approached ($\eta \to 0$), the instability threshold comes closer to the Rayleigh line. The unstable modes obtained in the analysis of the viscous case were non-axisymmetric and oscillatory, as those predicted by [30] in their inviscid study, and they were characterized by low azimuthal wavenumbers.

The first experimental evidence for SRI in the centrifugally stable regime was provided by [32]. They conducted their experiments at $Fr = 0.5$ and $\eta = 0.8$, a configuration that was similar to the narrow gap case considered by [22], and observed an instability threshold that was fully consistent with that obtained by these authors ($\mu \approx \eta$). From Kalliroscope visualizations, it was shown that the flow pattern consists of a superposition of two spiral modes that propagate

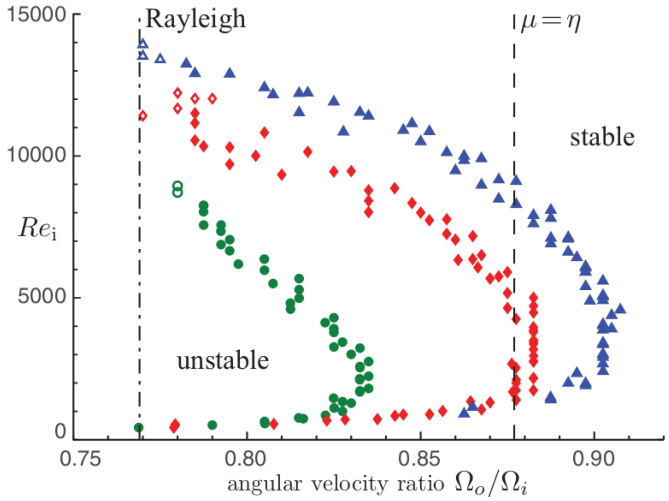

Figure 7. Critical stability boundary of SRI in the centrifugally stable regime obtained experimentally at three distinct values of the Brunt–Väisälä buoyancy frequency (reproduced from [34] with permission of the publisher): $N = 1.57s^{-1}$ (circles), $N = 3.14s^{-1}$ (diamonds) and $N = 4.71s^{-1}$ (triangles). The instability region grows with increasing N, i.e. as the fluid's stratification level increases. At a given value of $\mu = \Omega_o/\Omega_i$, the region of instability is bounded by two values of the inner cylinder Reynolds number, $Re_i = \Omega_i r_i d/\nu$.

axially in opposite directions (see figure. 6*c*). In accordance with the theoretical predictions, the structures were non-axisymmetric and oscillatory, rotating with a frequency equal to the mean angular velocity of the system. Their wavelengths, which did not change as μ was varied within the instability domain, were nearly the gap size, thereby confirming that stratification reduces the vertical extension of the structures in proportion to *Fr* (recall that the wavelength of the Taylor vortices in the non-stratified case is twice the gap size). Subsequent experiments by [34] extended the range of *Re* and *Fr* previously investigated. Their observations with respect to the structure of the unstable flow and its rotational frequency were in agreement with those of [32]. The experiments were conducted in a narrower configuration ($\eta = 0.88$), where instability was observed beyond $\mu = \eta$ (see figure 7), consistent with the prediction that the instability threshold approaches $\mu = 1$ as $\eta \to 1$. The critical threshold was also found to depend on the stratification level, moving towards larger values of μ as *Fr* decreases. They also reported an important characteristic which had been previously overlooked: the existence of a critical *Re* above which the flow restabilizes. It was observed that this critical *Re* value, and consequently the size of the instability domain, increases with increasing the stratification level (see figure 7). These observations were later confirmed by [23] in a combined experimental and theoretical study using a wider gap configuration with $\eta = 0.52$. It should be noted that in these latter experiments, the flow pattern was found to rotate slightly faster than the outer cylinder, which was in contrast with the experiments in [32] and [34], where the structures rotated with the mean angular velocity. This discrepancy appears to suggest that the rotation frequency of the flow pattern is affected by the curvature of the system and becomes slower in configurations with large curvature.

The physical mechanism underlying the instability was explained by [28] as a resonant interaction between Kelvin waves located at opposite boundaries (these are illustrated in figures 6*a*, obtained from linear stability analysis in [28], and 6*b*, obtained from PIV measurements in [31]). The other key ingredient of the instability is shear. This modifies the phase speeds of the Kelvin waves and creates a phase difference of nearly $90°$ between them. This phase shift results in an optimal correlation between the radial and azimuthal velocities that maximizes the energy growth rate (see equation 6 in [28]). Further discussion about this mechanism, which is widely accepted at present, is given in [20] and [25].

Although it has been speculated that SRI might play a major role in geophysical flows (both shear and Kelvin waves are omnipresent in nature), most studies so far were motivated by its potential relevance for astrophysical disks. Accretion in protostellar disks requires an efficient transport of angular momentum radially outward, which is only possible if the flow is turbulent. The source of this turbulence is however unclear [35]. Gases in accretion disks follow quasi-Keplerian rotation laws ($\mu \approx \eta^{1.5}$), which are centrifugally stable, and according to recent experiments and simulations, they also seem to be stable to finite amplitude disturbances [36–39]. While magnetic fields can destabilise the flow and produce accretion rates consistent with theoretical estimates through magneto-hydrodynamic instabilities [40,41], these instabilities cannot operate in cool disks, e.g. disks around young stars or in binary systems, because these are weakly ionized. The SRI emerged as a potential candidate to explain the presence of turbulence in these cases. Stable vertical stratification is present in accretion disks as a result of the illumination of the disk by the central object (a star or a planet) and the value of Fr associated with such stratification was estimated as $Fr \approx 3$ [30], a value that is consistent with those at which the instability is found in experiments and theoretical studies. A key question is whether SRI may transport angular momentum outward at the rates required for accretion to occur. Using fully nonlinear simulations of a temperature stratified Taylor–Couette flow, [24] quantified the outward angular momentum transport associated with the nonlinearly saturated state of SRI. Although these simulations were conducted at low Re ($Re \sim O(10^3)$), they extrapolated their results to real thin disks and obtained a turbulent viscosity of order unity, which was indicative of an efficient transport [42]. Several other studies have, however, questioned the applicability of SRI to real accretion disks. [43] found that SRI requires the presence of lateral boundaries to exist. If one or both boundaries are removed, the instability ceases to occur. A similar conclusion was reached by [20], who studied the stability of an unbounded Keplerian profile and observed that SRI is replaced by a radiative instability, with characteristics that substantially differ from those of SRI. The finding that there exist an upper bound for the rotation speed at which the instability occurs also seems to undermine the relevance of SRI for accretion disks. Experiments show that for $Fr \approx 3$, the upper bound of the instability is $Re \sim O(10^4)$ [34], which is very far from $Re > 10^9$ estimated for accretion disks [44]. It seems therefore very unlikely that this instability exists in real accretion disks.

Whether SRI causes turbulence is another aspect that remains unclear. With the exception of [28], where turbulence was found to occur following a well defined sequence of bifurcations, evidence of SRI-driven turbulence has not been reported in experiments or simulations. It should also be noted that the supercritical transition reported in [28] starts from stationary states which have not been observed in any subsequent study. The closest experimental observation of a turbulent state was reported by [34], who found a non-periodic state that quickly mixes the fluid near the upper part of the critical stability boundary (see open symbols in figure 7). However, such a state could not be characterized in detail, as the mixing rapidly destroys the axial density gradient and the flow laminarises. This problem is avoided when the stratification is accomplished via a stable vertical temperature gradient. Experiments and simulations using temperature stratification have been recently conducted [31,45] and some interesting nonlinear effects were reported at moderate value of Re. However, turbulence has so far not been observed in these cases either.

4. Perspective

Interests in stratified Taylor–Couette flows have ranged from understanding the fundamentals of the dynamics in a realizable laboratory flow, its relevance as a canonical example of the interplay between rotation, stable density stratification, velocity shear, and horizontal boundaries, to potential applications in geophysics and astrophysics.

Regarding the flows with only the inner cylinder rotating, the experiments and simulations described in the two cases considered in this review show that many instability mechanisms and bifurcation scenarios are possible, due to the large number of parameters involved. Many

more additional studies, both experimental and DNS are necessary in order to find and describe all these scenarios, in the same way that after one hundred years after G. I. Taylor's pioneering work on the Taylor–Couette problem there continues to be a steady flow of new studies in this classical problem. The experiments and DNS studies have shown that the role of endwalls cannot be neglected in any way, and play a fundamental role in the dynamics. We have also observed that with stratification the effects of centrifugal buoyancy may be critical in some scenarios, so it is convenient to include it in future studies.

There are many studies of stratified flows different from the stratified Taylor–Couette flows discussed in this perspective review, with a variety of instability mechanisms. A discussion of some of them and their relationship with the phenomena discussed in stratified Taylor–Couette flow follows.

The stable stratification in stratified Taylor–Couette flow inhibits bulk vertical motions, confining vertical motions primarily to the boundary layer on the rotating inner cylinder. In the wide gap case [17,18], the instability develops at the cylinder endwalls. Above a critical forcing amplitude (quantified by the inner-cylinder Reynolds number), the boundary layer loses stability to a complex pattern of helical waves with both senses of chirality (see figure 5). Similar consequences of stable stratification affecting boundary layer development and stability was also found in [46], where the boundary layer on a vertically oscillating wall of a rectangular container of stratified fluid underwent a similar helical instability. Stratification also restricts flows in the bulk (away from viscous boundaries) to internal waves associated with a forcing frequency if the system is periodically forced or to horizontal layers if the flow is steady. In comparing simulations or theory to experiments, the details of the container and the forcing mechanism matter. Idealizations ignoring, for example, endwalls lead to base states that are not compatible with the experimental boundary conditions and the resulting flows differ in significant ways.

Another startling phenomena not yet fully understood that occurs in sheared stratified flows is the formation of staircase horizontal layers in the vertical density profile; these are widely observed in many situations [47]. They have been observed in stratified Taylor–Couette flow in the medium gap case [6,7] (see figure 4). These structures also appear in stratified plane Couette flows. Stratified plane Couette flows have been studied using linear stability analysis of the idealized unidirectional flow, leading to instability modes that do not correspond well to the accompanying experiments, in which the flow is fully contained and the unidirectional base state does not correspond [48]; however, their nonlinear simulations that better account for the experimental confinement effects closely reproduce the experimental observations. Stratified plane Couette flows continue to be of interest, as other instability mechanisms such as Kelvin waves and inertia–gravity waves [49] appear, and in part because they result in density staircase horizontal layers. As noted by [50] however, stratified plane Couette flows remove two of the fundamental ingredients of Taylor–Couette flows: the effects of rotation and curvature. Other interesting stratified flows that also lack these ingredients but show different instability mechanisms are stratified plane Poiseuille flow [51], where instability results from a resonance of internal gravity waves and Tollmien-–Schlichting waves, and the stratified boundary layer flow on a vertical wall [52], where Tollmien-–Schlichting waves and radiative instability compete.

Regarding SRI in the centrifugally stable regime, future research should focus on the nonlinear development of the instability. These studies should clarify whether SRI driven turbulence exists or not, and in case it does, they should identify the parameter regimes for which this happens and the distinct transition pathways that emerge depending on the geometry of the apparatus and the relative importance between rotational and stratification effects. A good starting point would be understanding the reasons why the transition scenario reported in [28] has so far not been observed in experiments. Additional analysis [53] of the role of the endwalls in the nonlinear behaviour of the instability may help shed some light in this regard.

It should be noted that other instabilities associated with the stable stratification of accretion disks have been recently proposed, and so the study of stably stratified quasi-Keplerian flows continues to be an active focus of research. Prominent among these instabilities is the zombie

vortex instability [54–57], which has been found in numerical simulations of stratified rotating plane Couette flow. This instability arises when baroclinic critical layers, that exist in stably stratified flows [58], are excited by nearby vortices. As a result, the critical layers grow and roll up into new vortices, which in turn excite neighbouring critical layers. This process repeats until the disk is fully populated with vortices that interact to sustain turbulence. Although stably stratified Taylor–Couette flows include all the essential ingredients for the zombie vortex instability to occur (rotation, shear and stable stratification), no laboratory or observational evidence of the instability has been reported to date. Further research is thus needed to establish whether the instability exist in these flows and to assess its relevance for the outward angular momentum transport in accretion disks. The zombie vortex instability is inherently an inviscid instability of an unconfined flow, and so it too explicitly lacks some fundamental ingredients of Taylor–Couette flows: viscous boundary layers.

Authors' Contributions. Francisco Marques and Juan M. Lopez equally contributed to the first part (outer cylinder at rest) while Jose M. Lopez contributed to the second part (centrifugally stable flows) of the manuscript.

Competing Interests. The author(s) declare that they have no competing interests.

Funding. This work was supported by the Spanish Ministerio de Ciencia e Innovación grant PID2020-114043GB-100.

References

1. Taylor GI. 1923 Stability of a viscous liquid contained between two rotating cylinders. *Phil. Trans. R. Soc. A* **223**, 289–343.
2. Lopez JM, Marques F, Avila M. 2013 The Boussinesq approximation in rapidly rotating flows. *J. Fluid Mech.* **737**, 56–77.
3. Thorpe SA. 1966 The stability of stratified Couette flow. In *Notes on 1966 Summer Geophys. Fluid Dyn.* pp. 80–107. Woods Hole Oceanographic Inst.
4. Withjack EM, Chen CF. 1974 An experimental study of Couette instability of stratified fluids. *J. Fluid Mech.* **66**, 725–737.
5. Withjack EM, Chen CF. 1975 Stability analysis of rotational Couette flow of stratified fluids. *J. Fluid Mech.* **68**, 157–175.
6. Boubnov BM, Gledzer EB, Hopfinger EJ, Orlandi P. 1996 Layer formation and transitions in stratified circular Couette flow. *Dyn. Atmos. Oceans* **23**, 139–153.
7. Lopez JM, Marques F. 2022 Stratified Taylor-Couette flow: Nonlinear dynamics. *J. Fluid Mech.* **930**, A2.
8. Boubnov BM, Gledzer EB, Hopfinger EJ. 1995 Stratified circular Couette flow: instability and flow regimes. *J. Fluid Mech.* **292**, 333–358.
9. Hua BL, Le Gentil S, Orlandi P. 1997 First transitions in circular Couette flow with axial stratification. *Phys. Fluids* **9**, 365–375.
10. Caton F, Janiaud B, Hopfinger EJ. 1999 Primary and secondary Hopf bifurcations in stratified Taylor–Couette flow. *Phys. Rev. Lett.* **82**, 4647–4650.
11. Caton F, Janiaud B, Hopfinger EJ. 2000 Stability and bifurcations in stratified Taylor–Couette flow. *J. Fluid Mech.* **419**, 93–124.
12. Caulfield CP, Augier P, Le Bihan AC, Leclercq C, Partridge J. 2016 Turbulent layer dynamics in stratified Taylor–Couette flow. In Floryan JM, editor, *Contributions to the Foundations of Multidisciplinary Research in Mechanics* vol. 224*th Int. Congress of Theoretical and Applied Mechanics, 21–26 August 2016, Montreal, Canada* pp. 1447–1448. ISBN: NR16-127/2016E-EPUB.
13. Oglethorpe RLF, Caulfield CP, Woods AW. 2013 Spontaneous layering in stratified turbulent Taylor–Couette flow. *J. Fluid Mech.* **721**, R3.
14. Leclercq C, Partridge JL, Augier P, Caulfield CP, Dalziel SB, Linden PF. 2016a Nonlinear waves in stratified Taylor–Couette flow. Part 1. Layer formation. arXiv:1609.02885.
15. Leclercq C, Partridge JL, Caulfield CP, Dalziel SB, Linden PF. 2016b Nonlinear waves in stratified Taylor–Couette flow. Part 2. Buoyancy flux. arXiv:1609.02886.
16. Partridge JL, Leclercq C, Caulfield CP, Dalziel SB. 2016 Layer formation in stratified Taylor–Couette flow. In *VIIIth International Symposium on Stratified Flows* San Diego, USA.

17. Flór JB, Hirschberg L, Oostenrijk BH, van Heijst GJF. 2018 Onset of centrifugal instability at a rotating cylinder in a stratified fluid. *Phys. Fluids* **30**, 084103.
18. Lopez JM, Marques F. 2020 Impact of centrifugal buoyancy on strato-rotational instability. *J. Fluid Mech.* **890**, A9.
19. Riedinger X, Le Dizès S, Meunier P. 2011 Radiative instability of the flow around a rotating cylinder in a stratified fluid. *J. Fluid Mech.* **672**, 130–146.
20. Le Dizès S, Riedinger X. 2010 The strato-rotational instability of Taylor–Couette and Keplerian flows. *J. Fluid Mech.* **660**, 147–161.
21. Barcilon V, Pedlosky J. 1967 On the steady motions produced by a stable stratification in a rapidly rotating fluid. *J. Fluid Mech.* **29**, 673–690.
22. Shalybkov D, Rüdiger G. 2005 Stability of density-stratified viscous Taylor–Couette flows. *Astron. Astrophys.* **438**, 411–417.
23. Rüdiger G, Seelig T, Schultz M, Gellert M, Egbers C, Harlander U. 2017 The stratorotational instability of Taylor–Couette flows with moderate Reynolds numbers. *Geophys. Astrophys. Fluid Dyn.* **111**, 429–447.
24. Gellert M, Rüdiger G. 2009 Stratorotational instability in Taylor–Couette flow heated from above. *J. Fluid Mech.* **623**, 375–385.
25. Park J, Billant P. 2013 The stably stratified Taylor-Couette flow is always unstable except for solid-body rotation. *J. Fluid Mech.* **725**, 262–280.
26. Leclercq C, Nguyen F, Kerswell RR. 2016 Connections between centrifugal, stratorotational, and radiative instabilities in viscous Taylor–Couette flow. *Phys. Rev. E* **94**, 043103.
27. Park J, Billant P, Baik JJ, Seo JM. 2018 Competition between the centrifugal and strato-rotational instabilities in the stratified Taylor–Couette flow. *J. Fluid Mech.* **840**, 5–24.
28. Molemaker MJ, McWilliams JC, Yavneh I. 2001 Instability and equilibration of centrifugally stable stratified Taylor–Couette flow. *Phys. Rev. Lett.* **86**, 5270–5273.
29. Yavneh I, McWilliams JC, Molemaker MJ. 2001 Non-axisymmetric instability of centrifugally stable stratified Taylor–Couette flow. *J. Fluid Mech.* **448**, 1–21.
30. Dubrulle B, Marié L, Normand C, Richard D, Hersant F, Zahn JP. 2005 A hydrodynamic shear instability in stratified disks. *Astron. & Astrophys.* **429**, 1–13.
31. Seelig T, Harlander U, Gellert M. 2018 Experimental investigation of stratorotational instability using a thermally stratified system: instability, waves and associated momentum flux. *Geophys. Astrophys. Fluid Dyn.* **112**, 239–264.
32. Le Bars M, Le Gal P. 2007 Experimental analysis of the stratorotational instability in a cylindrical Couette flow. *Phys. Rev. Lett.* **99**, 064502.
33. Rüdiger G, Shalybkov DA. 2009 Stratorotational instability in MHD Taylor–Couette flows. *Astron. Astrophys.* **493**, 375–383.
34. Ibanez R, Swinney HL, Rodenborn B. 2016 Observations of the stratorotational instability in rotating concentric cylinders. *Phys. Rev. Fluids* **1**, 053601.
35. Ji H, Balbus S. 2013 Angular momentum transport in astrophysics and in the lab. *Physics Today* **66**, 27–33.
36. Ji H, Burin M, Schartman E, Goodman J. 2006 Hydrodynamic turbulence cannot transport angular momentum effectively in astrophysical disks. *Nature* **444**, 343–346.
37. Edlund EM, Ji H. 2014 Nonlinear stability of laboratory quasi-Keplerian flows. *Phys. Rev. E* **89**, 021004.
38. Edlund EM, Ji H. 2015 Reynolds number scaling of the influence of boundary layers on the global behavior of laboratory quasi-Keplerian flows. *Phys. Rev. E* **92**, 043005.
39. Lopez JM, Avila M. 2017 Boundary-layer turbulence in experiments on quasi-Keplerian flows. *J. Fluid Mech.* **817**, 21–34.
40. Balbus SA, Hawley JF. 1998 Instability, turbulence, and enhanced transport in accretion disks. *Rev. Mod. Phys.* **70**, 1–53.
41. Balbus SA. 2003 Enhanced angular momentum transport in accretion disks. *Annu. Rev. Astron. Astrophys.* **41**, 555–597.
42. Shakura NI, Sunyaev RA. 1973 Black holes in binary systems. Observational appearance.. *Astron. Astrophys.* **24**, 337–355.
43. Umurhan OM. 2006 On the stratorotational instability in the quasi-hydrostatic semigeostrophic limit. *Mon. Not. R. Astron. Soc.* **365**, 85–100.
44. Turner NJ, Fromang S, Gammie C, Klahr H, Lesur G, Wardle M, Bai XN. 2014 Transport and accretion in planet-forming disks. *Arizona University press*.

45. Meletti G, Abide S, Viazzo S, Krebs A, Harlander U. 2021 Experiments and long-term high-performance computations on amplitude modulations of strato-rotational flows. *Geophys. Astrophys. Fluid Dyn.* **115**, 297–321.
46. Yalim J, Welfert BD, Lopez JM. 2022 Oblique instability of a stratified oscillatory boundary layer. *J. Fluid Mech.* **933**, R3.
47. Caulfield CP. 2021 Layering, Instabilities, and Mixing in Turbulent Stratified Flows. *Annu. Rev. Fluid Mech.* **53**, 113–145.
48. Facchini G, Favier B, Le Gal P, Wang M, Le Bars M. 2018 The linear instability of the stratified plane Couette flow. *JFM* **853**, 205–234.
49. Vanneste J, Yavneh I. 2007 Unbalanced instabilities of rapidly rotating stratified shear flows. *J. Fluid Mech.* **584**, 373–396.
50. Lucas D, Caulfield CP, Kerswell RR. 2019 Layer formation and relaminarisation in plane Couette flow with spanwise stratification. *J. Fluid Mech.* **868**, 97–118.
51. Le Gal P, Harlander U, Borcia ID, Le Dizès S, Chen J, Favier B. 2021 Instability of vertically stratified horizontal plane Poiseuille flow. *J. Fluid Mech.* **907**, R1.
52. Chen J, Bai Y, Le Dizès S. 2016 Instability of a boundary layer flow on a vertical wall in a stably stratified fluid. *J. Fluid Mech.* **795**, 262–277.
53. Leclercq C, Partridge JL, Augier P, Dalziel SB, Kerswell RR. 2016 Using stratification to mitigate end effects in quasi-Keplerian Taylor–Couette flow. *J. Fluid Mech.* **791**, 608–630.
54. Marcus PS, Pei S, Jiang CH, Hassanzadeh P. 2013 Three-Dimensional Vortices Generated by Self-Replication in Stably Stratified Rotating Shear Flows. *Phys. Rev. Lett.* **111**, 084501.
55. Marcus PS, Pei S, Jiang CH, Barranco JA, Hassanzadeh P, Lecoanet D. 2015 Zombie Vortex Instability. I. A Purely Hydrodynamic Instability to Resurrect the Dead Zones of Protoplanetary Disks. *The Astrophysical Journal* **808**, 87.
56. Marcus PS, Pei S, Jiang CH, Barranco JA. 2016 Zombie Vortex Instability. II. Thresholds to Trigger Instability and the Properties of Zombie Turbulence in the Dead Zones of Protoplanetary Disks. *The Astrophysical Journal* **833**, 148.
57. Barranco JA, Pei S, Marcus PS. 2018 Zombie Vortex Instability. III. Persistence with Nonuniform Stratification and Radiative Damping. *The Astrophysical Journal* **869**, 127.
58. Boulanger N, Meunier P, Le Dizès S. 2008 Tilt-induced instability of a stratified vortex. *Journal of Fluid Mechanics* **596**, 1–20.